Received: 7 July 2020 | Revised: 28 November 2020 | Accepted: 4 January 2021

DOI: 10.1049/rpg2.12123

IET Renewable Power Generation

The Institution of Engineering and Technology WILEY

ORIGINAL RESEARCH PAPER

Sensorless MRAS control of emerging doubly-fed reluctance wind generators

Mohammad-Reza Agha-Kashkooli | **Milutin Jovanović**

Faculty of Engineering and Environment, Northumbria University Newcastle, Newcastle upon Tyne, UK

Correspondence
Mohammad-Reza Agha-Kashkooli, Faculty of Engineering and Environment, Northumbria University Newcastle, Newcastle upon Tyne, UK.
Email: mohammad.kashkooli@northumbria.ac.uk

Abstract

A new model reference adaptive system based estimation technique for vector control of real and reactive power of a brushless doubly fed reluctance generator without a shaft position sensor is proposed. The rotor speed is being precisely observed in a closed-loop manner by eliminating the error between the measured and estimated inverter-fed (secondary) winding current angles in a stationary frame. Contrary to the existing model reference adaptive system observer designs reported in the brushless doubly fed reluctance generator literature, the reference model is entirely parameter-free and only utilises direct measurements of the secondary currents. Furthermore, the current estimates coming from the adaptive model are obtained using the measured voltages and currents of the grid-connected (primary) winding, which has provided prospects for much higher accuracy and superior overall performance. The realistic simulations, preliminary experimental results, and the accompanying parameter sensitivity studies have shown the great controller potential for typical operating conditions of variable speed wind turbines with maximum power point tracking.

1 | INTRODUCTION

A conventional slip-ring doubly fed induction generator (DFIG), and its brushless alternative (BDFG), allow the use of a partially-rated power converter in wind power applications, which is not only low cost but also more reliable than a fully-rated counterpart of electrically-excited or permanent magnet synchronous generators [1, 2]. The BDFG is an attractive maintenance-free solution and it overcomes the main DFIG limitations by the absence of brush gear. It has two standard sinusoidally distributed stator windings of different pole numbers and applied frequencies as shown in Figure 1. The primary is connected to a fixed voltage and frequency grid, whereas the secondary is back-to-back converter fed at controllable voltage and frequency. The bi-directional power flow on the secondary side enables the BDFG operation in super- or sub-synchronous speed modes. The indirect magnetic coupling between the windings for the torque production is provided by the rotor with the pole number equal to the sum of the stator pole-pairs [3]. This makes the BDFG 'natural' synchronous speed half that of the equivalent DFIG. Hence, a more efficient, compact medium speed two-stage gearbox can be used for BDFG turbines [4, 5] bringing significant reliability and economic advantages over DFIG drive trains using a complicated three-stage one [6]. Furthermore, the BDFG has been proven to have superior low voltage fault ride through capabilities to DFIG due to the relatively higher leakage inductances [7, 8], as well as the potential for competitive frequency support provision [9].

A modern cage-less reluctance rotor version of the BDFG, the brushless doubly-fed reluctance generator (BDFRG), presented in Figure 1 is particularly promising [10, 11]. It can offer better efficiency, facilitated less parameter dependent dynamic modelling and much simpler control compared to the cage induction rotor counterpart with nested-loop structures [12–14]. The latest state-of-the-art hybrid reluctance rotor designs with assistive conductive bars have augmented further the torque density and efficiency [15].

Two distinct control concepts have been considered for the BDFRG [16]: hysteresis control (HC) [17, 18], and vector control (VC) [19, 20]. Variable switching rates and higher total harmonic distortion are the known drawbacks of direct power HC strategies. VC can resolve these issues offering superior

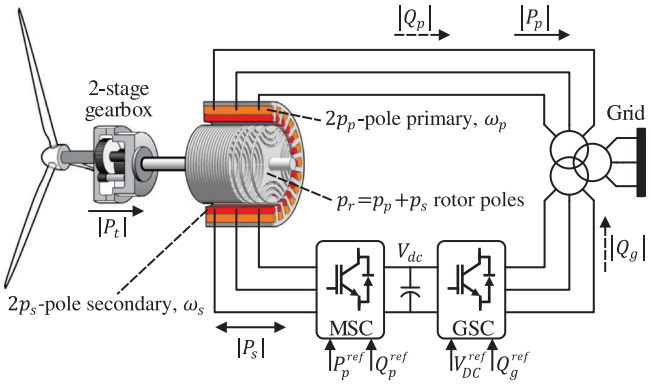

FIGURE 1 A BDFRG-based wind energy conversion system schematic

power quality and has been widely adopted for wind energy conversion systems (WECS). However, the utilisation of shaft encoders for voltage or flux oriented VC undermines the mechanical robustness and reliability. The development of rotor position and/or speed estimation techniques for sensorless operation of both DFIG [21–24] and BDFRG [25–28] has been getting increasingly popular for this reason.

A Luenberger observer has been effectively used to estimate the rotor speed and position for field oriented control (FOC) of the BDFRG [25, 26]. However, this method is highly parameter dependent, and sensitivity analyses have not been done. The alternative MRAS speed observers with the same dedicated controller as in ref. [25] are presented in refs. [27–29]. The secondary-flux estimation is prone to the well-known back-emf integration errors caused by the more pronounced resistive effects at low fundamental frequency converter voltages and currents in much the same manner as with the rotor winding of DFIGs [21]. For this reason, it has been unable to guarantee the controller stability over the entire speed range [27]. Using the secondary reactive [28] or real power [29] as the reference model basis has improved the MRAS observer performance. However, the adaptive model in ref. [28] relies on all self and mutual inductances of the machine, being particularly sensitive to the secondary one, which is difficult to determine accurately by off-line testing due to the large leakage of the BDFRG secondary winding [30]. In contrast, the real power based MRAS presented in ref. [29] requires only the secondary resistance (R_s) and mutual inductance knowledge. As such, it is less parameter dependent than that in ref. [28]. However, the parameter sensitivity analysis is only performed to R_s variations, but not to the mutual inductance uncertainties, the latter being crucial for the observer performance. The MRAS observer designs in refs. [31, 32] bring additional advantages by introducing the measurable secondary currents as the reference model outputs, while the corresponding estimates are entirely based on the primary quantities at fixed line frequency. However, the requirement for the flux identification and resistance (R_p) knowledge of the primary winding is the main drawback of the adaptive models in refs.[31, 32]. Furthermore, the associated results are produced for a small BDFRG prototype with relatively limited industrial interest for wind power applications.

TABLE 1 The BDFRG wind turbine: Parameters and Ratings

Parameter	Value
Power (MW)	1.5
Primary voltage (V rms)	$V_p = 690$
Secondary voltage (V rms)	$V_s = 230$
Primary current (kA rms)	$I_p = 1.1$
Secondary current (kA rms)	$I_s = 1.2$
Stator resistance (mΩ)	$R_p = 7$, $R_s = 14.2$
Stator self-inductance (mH)	$L_p = 4.7$, $L_s = 5.7$
Mutual inductance (mH)	$L_m = 4.5$
Stator pole-pairs	$p_p = 4$, $p_s = 2$
Winding connections	Y/Y
Generator speed (rev/min)	$n_{rm} = 30\omega_{rm}/\pi = 600$
Turbine speed (rev/min)	$n_t = 30\omega_t/\pi = 20$
Gearbox ratio	$g = 30$

This paper presents a novel rotor angular velocity and position MRAS observer for encoder-less vector control of the grid-connected BDFRG. A simpler implementation and inferior parameter sensitivity are achieved in comparison with the state observer in refs.[25, 26]. The absence of troublesome secondary flux estimation in the low frequency region makes it clearly superior to that in ref. [27]. The measured secondary current stationary-frame components used as the reference model outputs can provide higher reliability and fewer parameter dependence than the MRAS observers in refs.[28, 29]. Moreover, the proposed primary power based adaptive model design overcomes the limitations of the counterparts in refs. [31, 32] by avoiding the primary voltage integration issues and the need for R_p in flux calculations, hence offering improved accuracy and easier implementation. The small-signal analysis of the parameter mismatches and the excellent controller response are supported by the realistic simulation and experimental studies of a large-scale wind turbine.

2 | BDFRG OPERATION

The key rotor angular velocity and position relationships for the BDFRG with the ω_p supply frequency of the primary and ω_s for the secondary winding, can be written as [19, 20, 25]:

$$\omega_{rm} = \frac{\omega_p + \omega_s}{p_r} = \frac{\omega_p}{p_r}\left(1 + \frac{\omega_s}{\omega_p}\right) = \omega_{syn}\left(1 + \frac{\omega_s}{\omega_p}\right), \quad (1)$$

$$\theta_{rm} = \frac{\theta_p + \theta_s}{p_p + p_s} = \frac{\theta_p + \theta_s}{p_r}, \quad (2)$$

where p_p and p_s denote the windings pole pairs, and $p_r = p_p + p_s$ is the rotor poles number. Figure 2 illustrates the meanings of θ_p and θ_s reference frames angles in Equation (2). When the secondary is DC (i.e $\omega_s = 0$), the BDFRG operates in

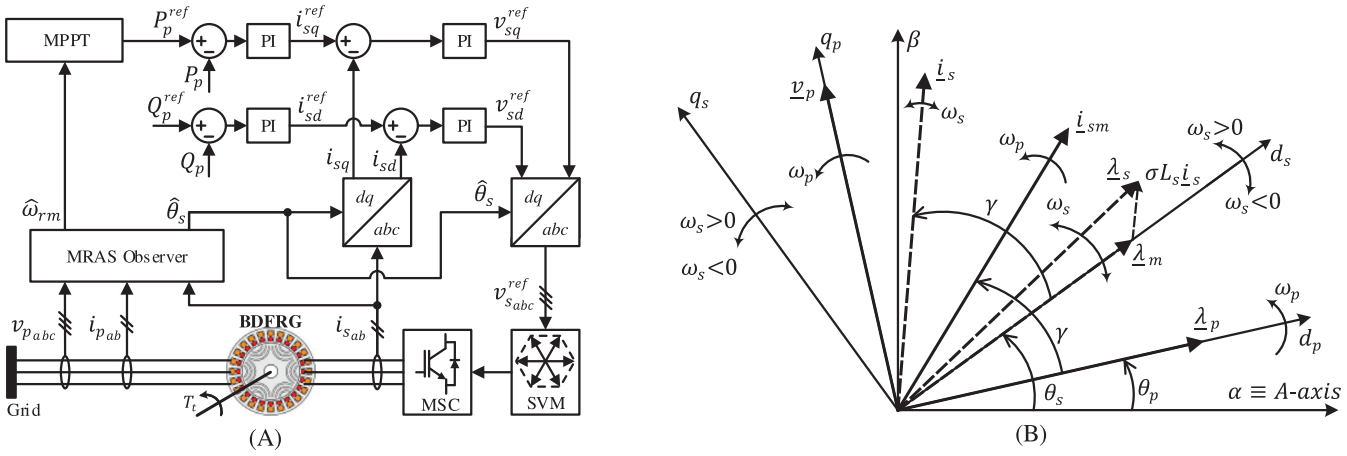

FIGURE 2 The BDFRG sensorless primary-voltage oriented controller: (A) Block scheme; (B) Phasor diagram

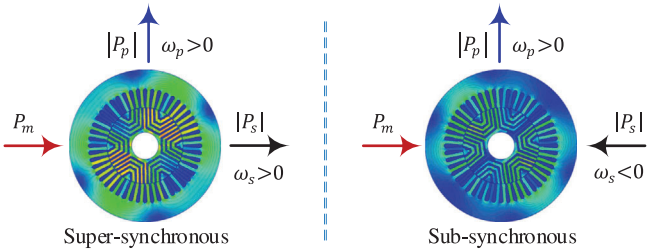

FIGURE 3 Reference power flow and field distribution in the simulated 8/4-pole BDFRG with a 6-pole multi-barrier rotor design [9]

synchronous mode at ω_{syn}, which is half that of a p_r-pole DFIG given Equation (1). Thus, the BDFRG can be classified as a medium-speed machine requiring a two-stage gearbox unlike the vulnerable three-stage one with DFIG wind turbines [33].

The mechanical power input of the BDFRG for the maximum wind energy extraction in steady-state can be expressed using Equation (1) as follows:

$$P_m = T_e \cdot \omega_{rm} = \underbrace{\frac{T_e \cdot \omega_p}{p_r}}_{P_p} + \underbrace{\frac{T_e \cdot \omega_s}{p_r}}_{P_s} = P_s \cdot \left(1 + \frac{\omega_p}{\omega_s}\right), \quad (3)$$

where the electro-magnetic torque ($T_e < 0$) and the primary power ($P_p < 0$) with the assumed motoring (BDFRM) convention. The bi-directional flow of the secondary power (P_s) allows the machine operation above and below the synchronous speed, i.e. in super-synchronous mode ($\omega_s > 0$) when $P_s < 0$, and at sub-synchronous speeds ($\omega_s < 0$) for $P_s > 0$ as shown in Figure 3.

If a variable speed range of the BDFRG wind turbine is symmetric around ω_{syn}, i.e. $[\omega_{min} = \omega_{syn} - \Delta\omega_r, \omega_{max} = \omega_{syn} + \Delta\omega_r]$, it can be defined by the following ratio:

$$r = \frac{\omega_{max}}{\omega_{min}} = \frac{\omega_p + \omega_s}{\omega_p - \omega_s} \Longrightarrow \frac{\omega_s}{\omega_p} = \frac{r-1}{r+1}. \quad (4)$$

Therefore, for a typical $r = 2$, the secondary frequency is limited to $\omega_s = \omega_p/3$ and $P_s \approx 0.25P_m$ from Equation (3). This implies that a fractional converter can be used by analogy to DFIG.

3 | DYNAMIC MODELLING AND CONTROL

The BDFRG(M) $d-q$ model in rotating reference frames (Figure 2(B)) can be represented by the following set of equations using standard space vector notation [19, 20]:

$$\underline{v}_p = R_p \underline{i}_p + \frac{d\underline{\lambda}_p}{dt} + j\omega_p \underline{\lambda}_p, \quad (5)$$

$$\underline{v}_s = R_s \underline{i}_s + \frac{d\underline{\lambda}_s}{dt} + j\omega_s \underline{\lambda}_s, \quad (6)$$

$$\underline{\lambda}_p = L_p \underline{i}_p + L_m \underline{i}^*_{sm} = L_p(i_{pd} + ji_{pq}) + L_m(i_{md} - ji_{mq}), \quad (7)$$

$$\underline{\lambda}_s = L_s \underline{i}_s + L_m \underline{i}^*_{pm} = \sigma L_s \underline{i}_s + \frac{L_m}{L_p}\underline{\lambda}^*_p = \sigma L_s \underline{i}_s + \underline{\lambda}_m, \quad (8)$$

$$T_e = \frac{3}{2}p_r\left(\lambda_{pd} i_{pq} - \lambda_{pq} i_{pd}\right) = \frac{3}{2}p_r\left(\lambda_{md} i_{sq} - \lambda_{mq} i_{sd}\right), \quad (9)$$

where L_m is the magnetising inductance, L_p and L_s are the primary and secondary self-inductances, $\sigma = 1 - L_m^2/(L_p L_s)$ is the leakage coefficient, λ_m is the mutual flux linkage, and the superscript '*' denotes complex conjugate [34].

It is important to emphasise that ω_p rotating $\underline{i}_{sm}$ is the frequency (but not amplitude) modulated secondary current vector ($\underline{i}_s$) running at ω_s as shown in Figure 2(B). Furthermore, the relative angular displacements and magnitudes of $\underline{i}_{sm}$ and $\underline{i}_s$ from the respective flux vectors $\underline{\lambda}_p$ and $\underline{\lambda}_m$ are the same so the following relationship applies in the corresponding reference frames under FOC conditions (i.e. with the d_p-axis aligned with $\underline{\lambda}_p$, and

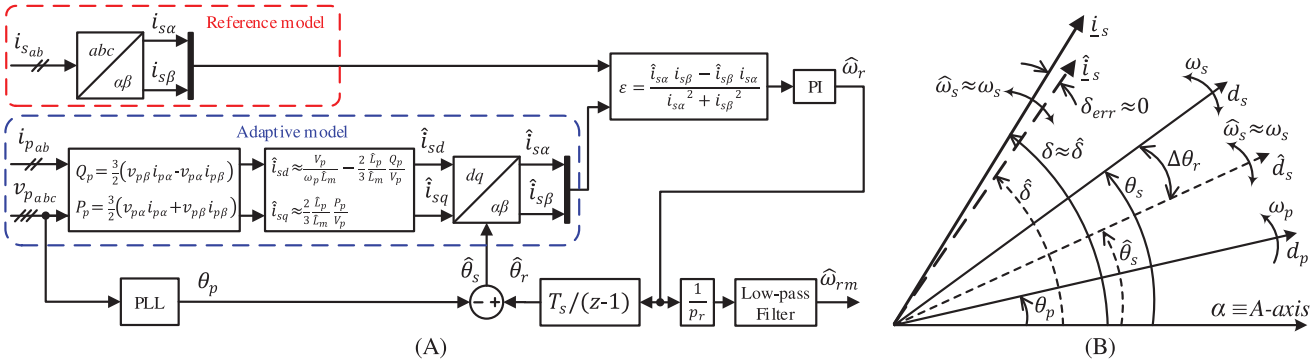

FIGURE 4 The proposed MRAS observer: (A) Block scheme; (B) Phasor diagram

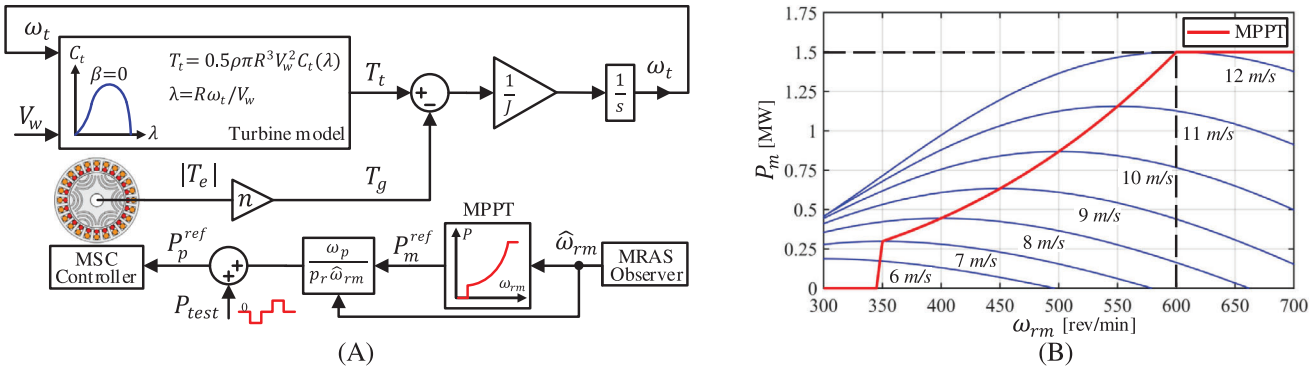

FIGURE 5 (A) Aerodynamic and mechanical WECS models; (B) Turbine output power and Maximum Power Point Tracking (MPPT) curve

the d_s-axis with $\underline{\lambda}_m$) [19, 20, 25]:

$$\underbrace{\underline{i}_{sm} = i_{md} + ji_{mq} = i_{sm}e^{j\gamma}}_{d_p-q_p\text{frame}} \Leftrightarrow \underbrace{\underline{i}_s = i_{sd} + ji_{sq} = i_s e^{j\gamma}}_{d_s-q_s\text{frame}}. \quad (10)$$

The fundamental power expressions, $P_p = 1.5 \cdot \text{Re}\{\underline{v}_p \underline{i}_p^*\}$ and $Q_p = 1.5 \cdot \text{Im}\{\underline{v}_p \underline{i}_p^*\}$, can be simplified by aligning the q_p-axis with the primary voltage vector (i.e $v_{pq} = v_p$, $v_{pd} = 0$) as depicted in Figure 2. Hence, $P_p = 1.5 v_p i_{pq}$ and $Q_p = 1.5 v_p i_{pd}$. However, as i_{pd} and i_{pq} are the $d_p - q_p$ frame components and cannot be varied directly, P_p and Q_p should be expressed in terms of the corresponding controllable secondary current counterparts, i_{sd} and i_{sq} in the $d_s - q_s$ frame. Neglecting the winding resistance (R_p), which is a valid approximation for large generators, the key FOC form relations can be developed by using Equations (5) and (7) with $\lambda_{pd} \approx \lambda_p = v_p/\omega_p$, $\lambda_{pq} \approx 0$, and $i_{md} = i_{sd}$ and $i_{mq} = i_{sq}$ from Equation (10):

$$P_p = \frac{3}{2} v_p i_{pq} = \frac{3}{2} \frac{\lambda_{pq} + L_m i_{mq}}{L_p} v_p \approx \frac{3}{2} \frac{L_m}{L_p} v_p i_{sq}, \quad (11)$$

$$Q_p = \frac{3}{2} v_p i_{pd} = \frac{3}{2} \frac{\lambda_{pd} - L_m i_{md}}{L_p} v_p \approx \frac{3 v_p}{2 L_p} \left(\frac{v_p}{\omega_p} - L_m i_{sd} \right), \quad (12)$$

Note that ignoring R_p not only allows straightforward, yet reasonably accurate, calculations of the primary flux magnitude ($\lambda_p \approx v_p/\omega_p$), but significant simplifications, and a faster execution, of the observer-control algorithm by avoiding to deal with the voltage integration issues (e.g. dc offset) to identify λ_{pq} and λ_{pd} in Equations (11) and (12). Furthermore, since v_p and ω_p are both constant, P_p and Q_p can be controlled in an inherently decoupled manner through i_{sq} and i_{sd} respectively as illustrated in Figure 2(A). The inductance knowledge is not required for this purpose as any uncertainties can be effectively taken care of by the properly tuned PI regulators as will be shown by the results presented in Section 5.

4 | MRAS OBSERVER DESIGN

In a MRAS observer, the rotor speed information is retrieved by comparing the actual state variables and their rotor position dependent estimates generated by the reference and adaptive models, respectively. A suitable adaptation mechanism is devised to drive the differential between the models outputs to zero, which is a prerequisite for the algorithm to converge. Hence, an accurate speed estimation is possible in a stable, closed-loop fashion [35].

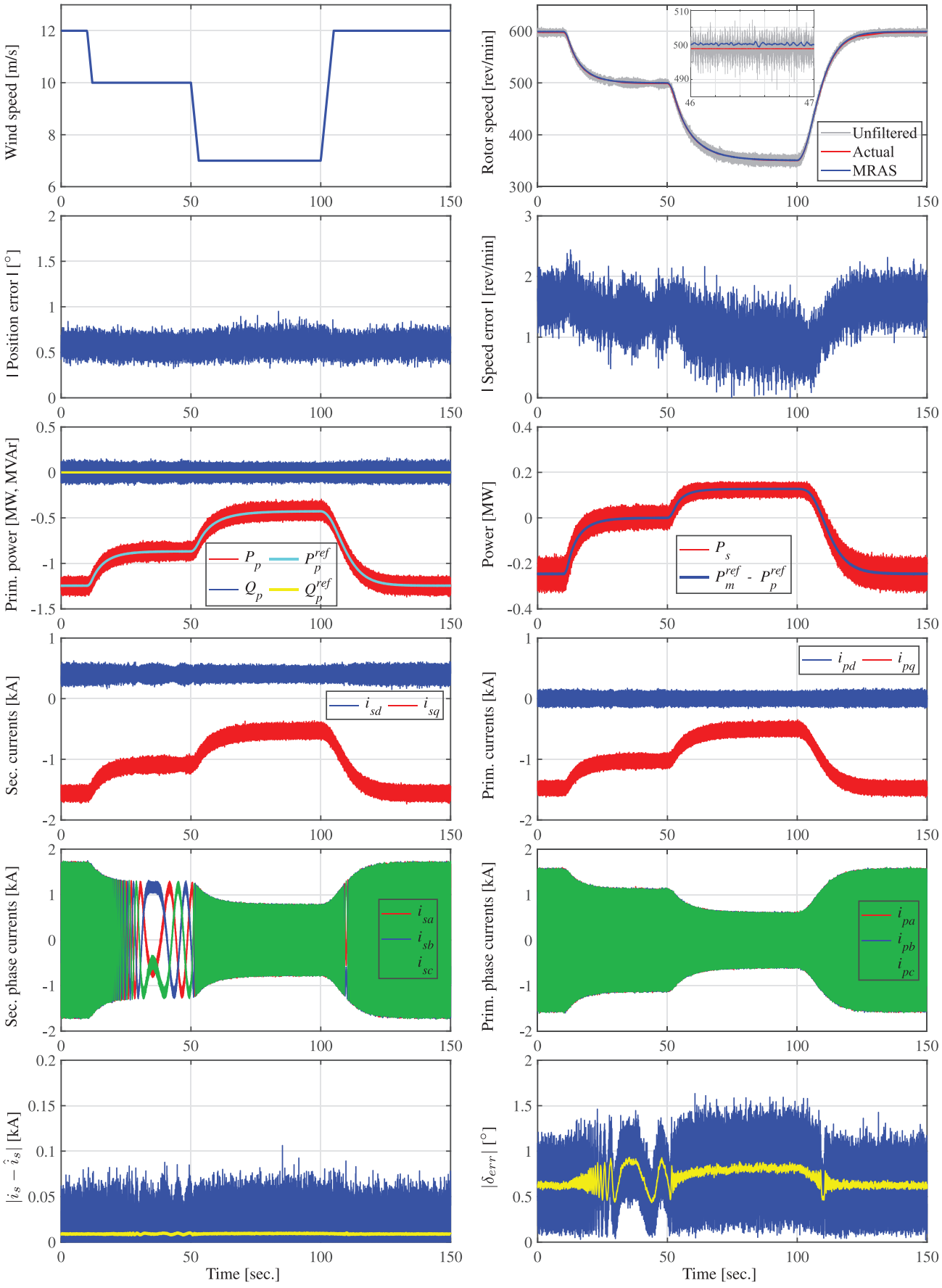

FIGURE 6 Sensorless operation of the grid-connected BDFRG wind turbine with MRAS observer based MPPT and reactive power control

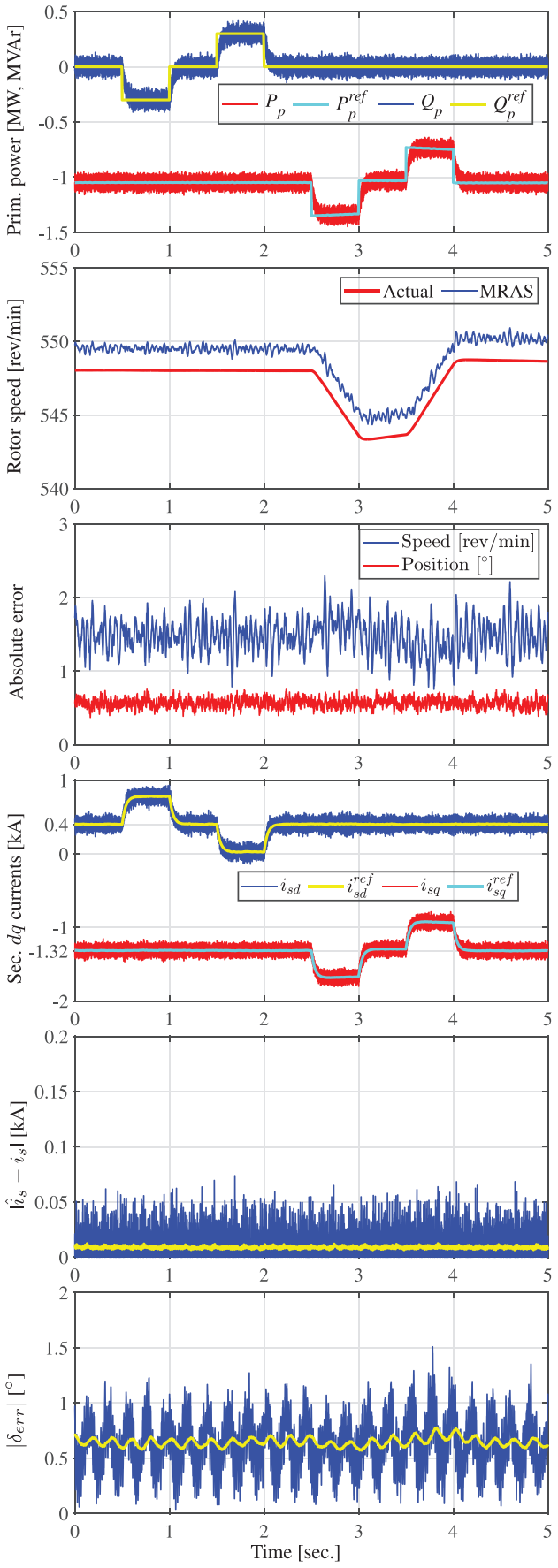

FIGURE 7 Observer response to power surges at 11 m/s wind speed

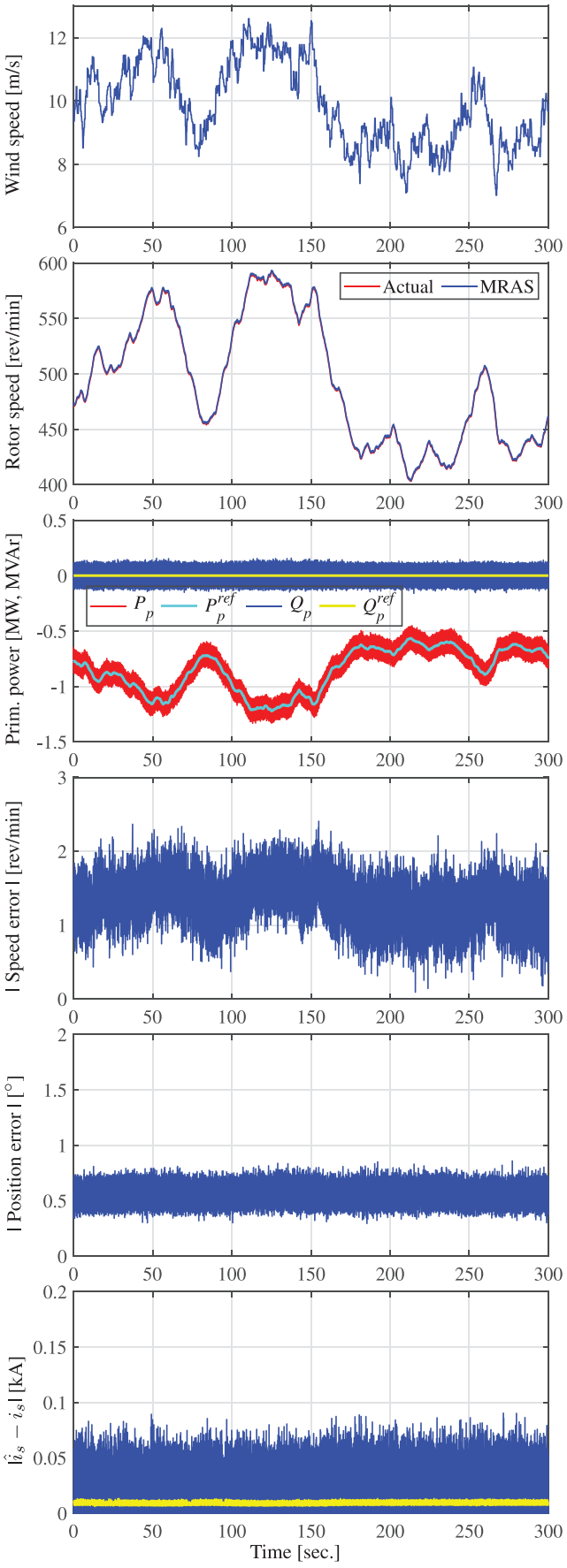

FIGURE 8 BDFRG performance for a realistic wind speed profile.

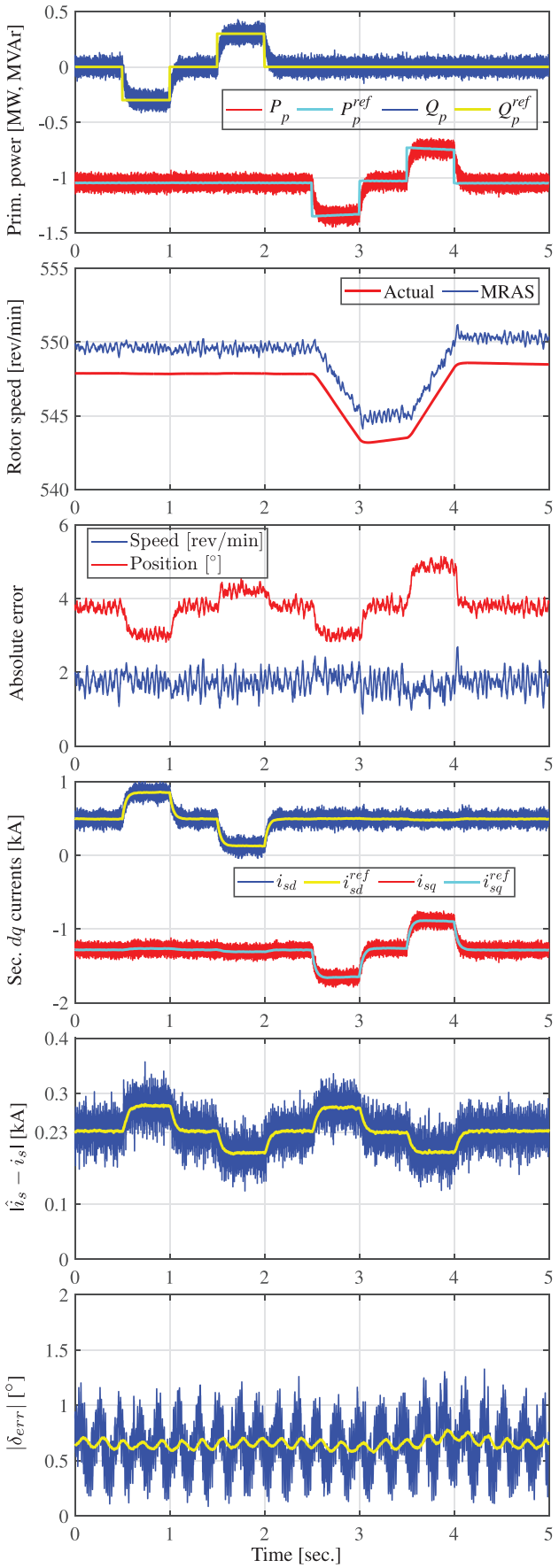

FIGURE 9 Parameter mismatch: $\hat{L}_m = 0.7\ L_m$, $\hat{L}_p = 0.8\ L_p$

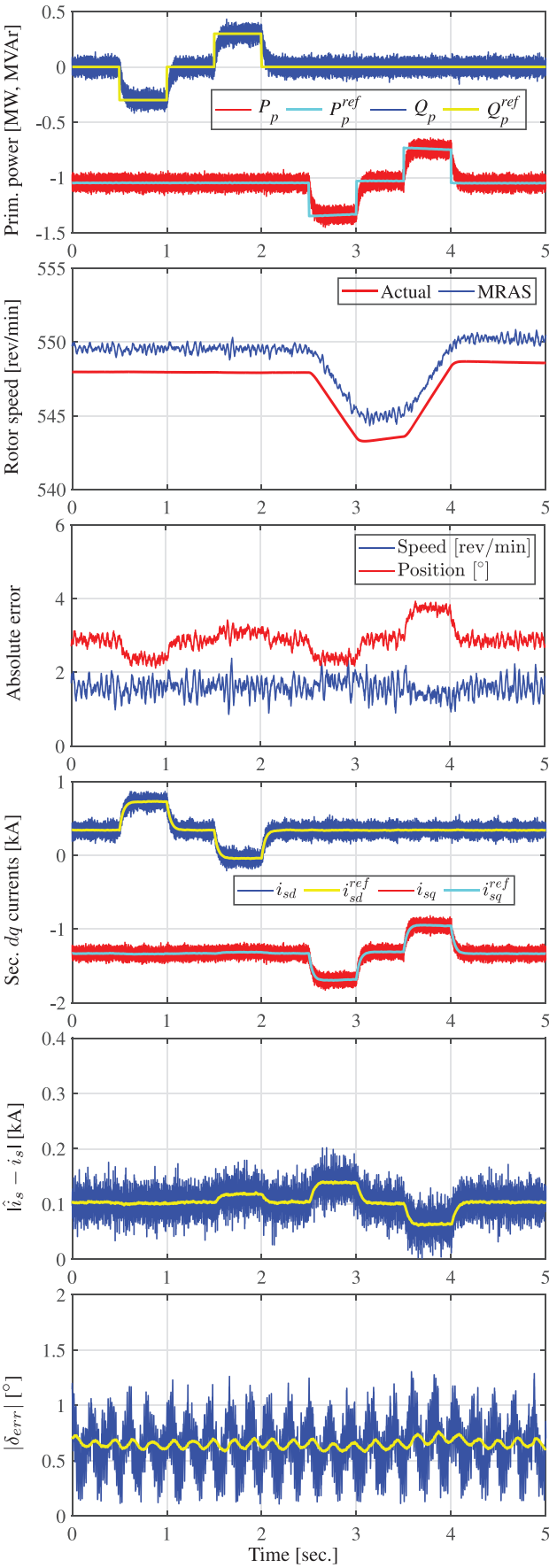

FIGURE 10 Parameter mismatch: $\hat{L}_m = 1.1\ L_m$, $\hat{L}_p = 1.2\ L_p$

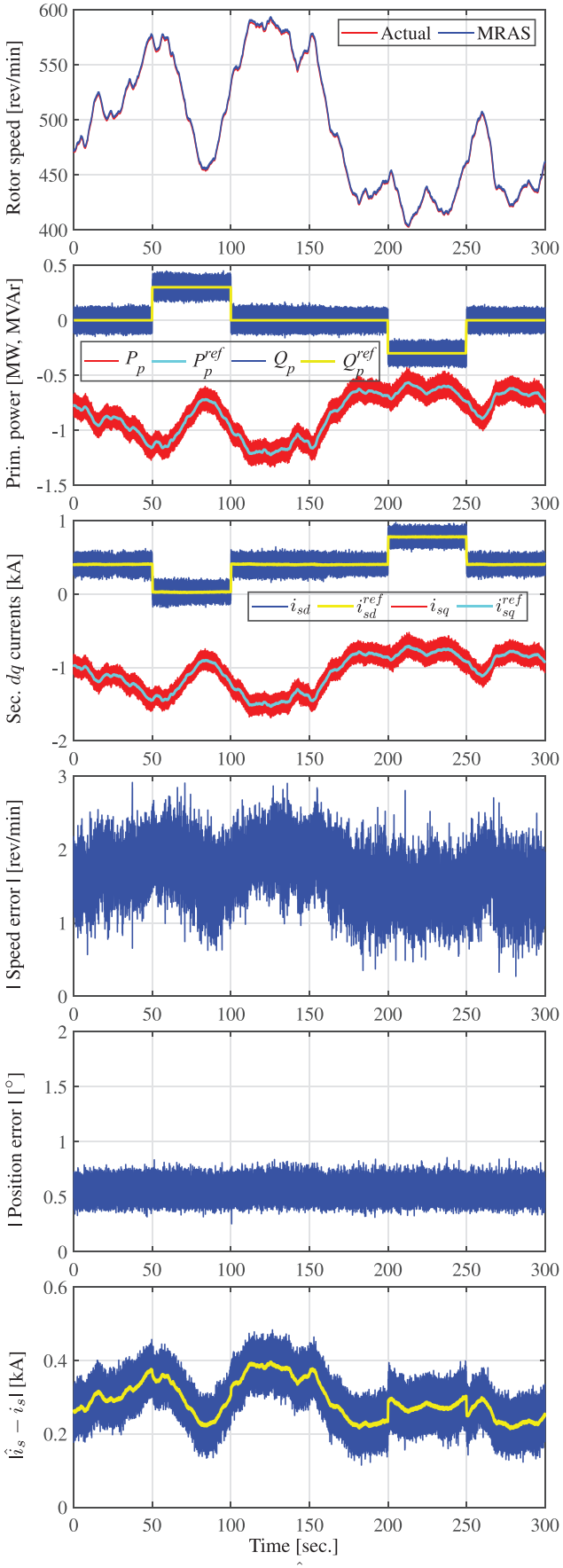

FIGURE 11 L_{m} mismatch studies: $\hat{L}_{\mathrm{m}} = 0.8\, L_{\mathrm{m}}, \hat{L}_{\mathrm{p}} = L_{\mathrm{p}}$

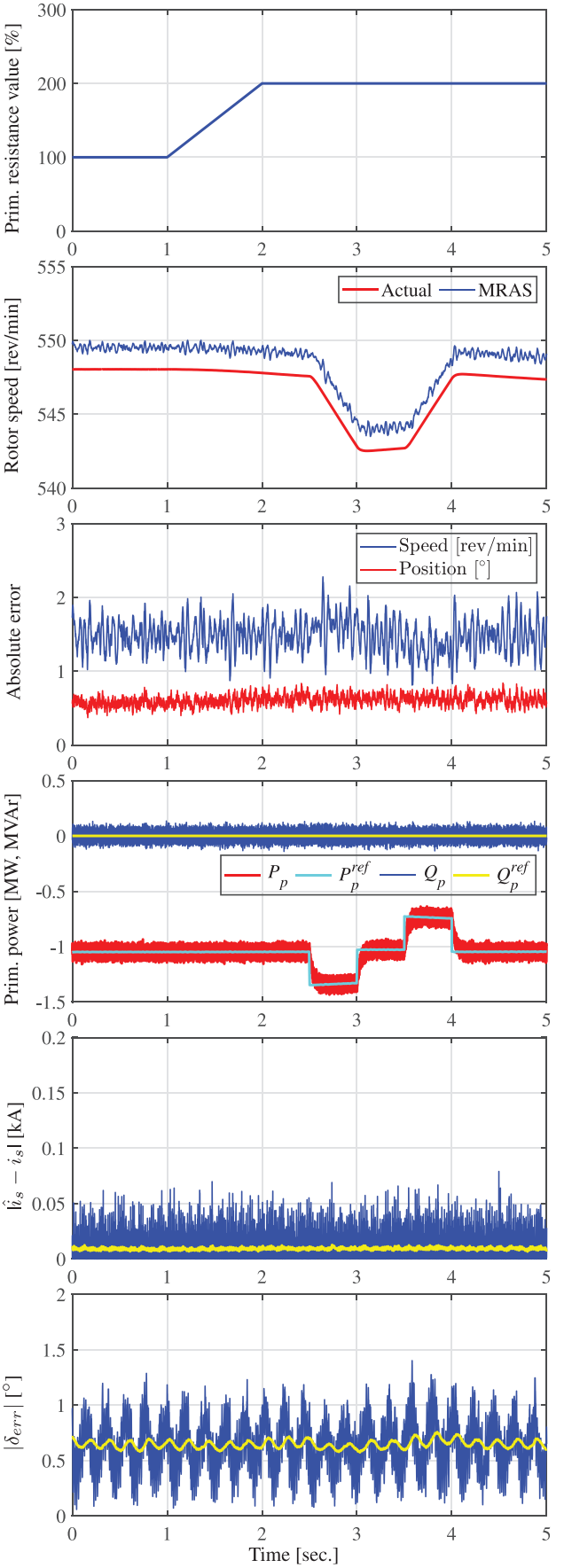

FIGURE 12 Primary resistance variation by 200% at 11 m/s wind speed

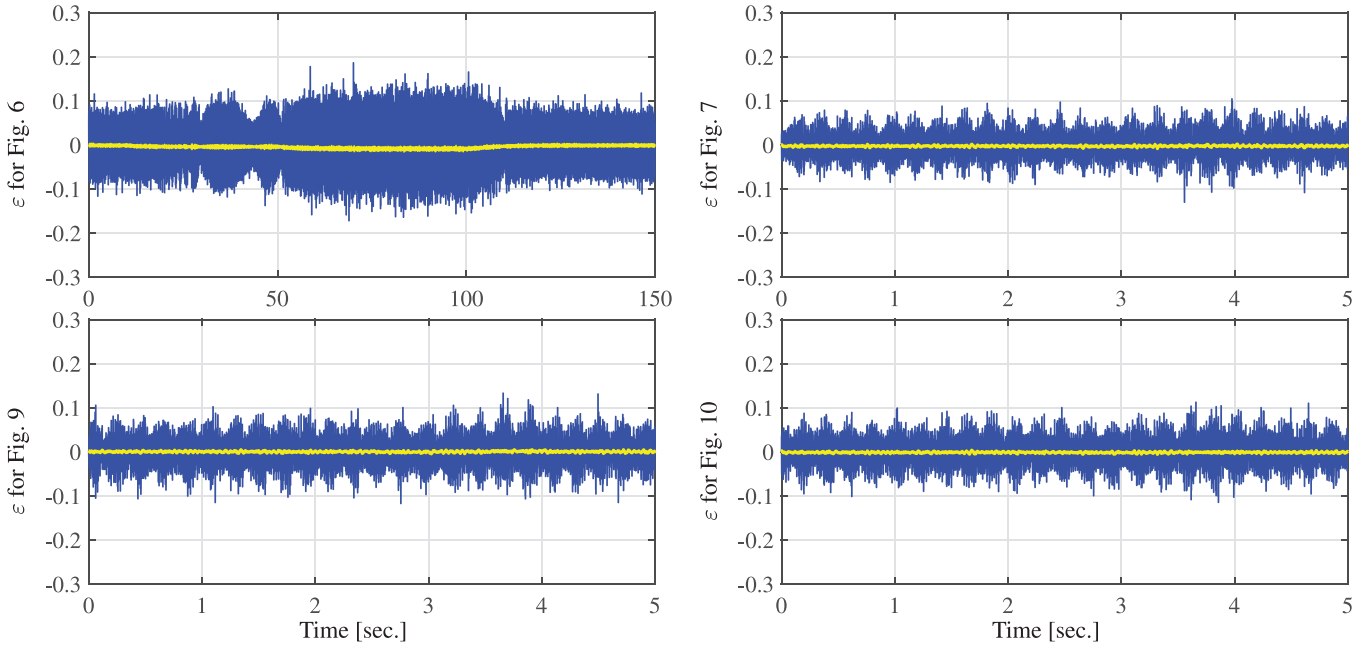

FIGURE 13 The error between the reference and adaptive model outputs (ε) under different test conditions

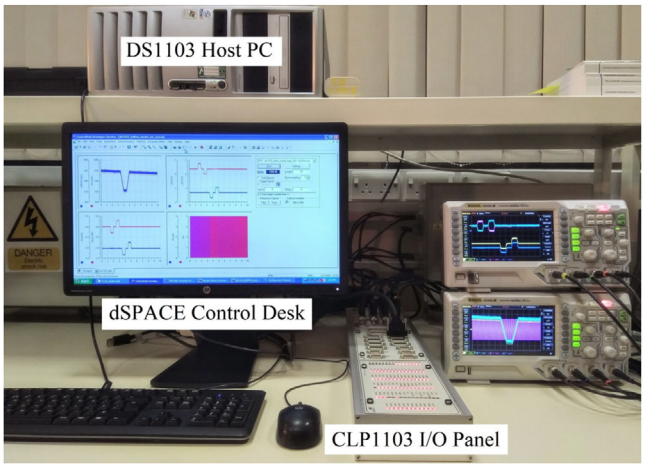

FIGURE 14 A HIL apparatus for the BDFRG wind turbine emulation

4.1 | Reference and adaptive models

The proposed MRAS observer layout is presented in Figure 4(A). The secondary current components in a stationary $\alpha-\beta$ frame are used as the reference model outputs. The obvious advantages of such a selection are the complete parameter independence and high current sensor-alike accuracy afforded by the immediately accessible $i_{s\alpha}$ and $i_{s\beta}$ from measurements. For a star-connected secondary winding with a positive phase sequence and an isolated neutral point, the latter can be calculated as:

$$\underline{i}_s = i_s e^{j\delta} = i_{s\alpha} + j i_{s\beta} = i_{sa} + j\frac{i_{sa}+2i_{sb}}{\sqrt{3}}. \tag{13}$$

Under the FOC conditions according to Equation (10), the magnetically coupled secondary currents in the ω_p frame, $\hat{i}_{mq}$ and $\hat{i}_{md}$, are mirror images of the actual ones in the ω_s frame, $\hat{i}_{sq}$ and $\hat{i}_{sd}$, and they can be estimated from the measured P_p and Q_p using Equations (11) and (12):

$$\hat{i}_{mq} = \hat{i}_{sq} \approx \frac{\hat{L}_p}{v_p \hat{L}_m}\underbrace{(v_{p\alpha} i_{p\alpha} + v_{p\beta} i_{p\beta})}_{\frac{2}{3}P_p}, \tag{14}$$

$$\hat{i}_{md} = \hat{i}_{sd} \approx \frac{v_p}{\omega_p \hat{L}_m} - \frac{\hat{L}_p}{v_p \hat{L}_m}\underbrace{(v_{p\beta} i_{p\alpha} - v_{p\alpha} i_{p\beta})}_{\frac{2}{3}Q_p}, \tag{15}$$

where $\hat{L}_m$ and $\hat{L}_p$ are the inductance estimates and (Figure 2(B)):

$$\underline{v}_p = v_p e^{j(\theta_p+\pi/2)} = v_{p\alpha} + j v_{p\beta} = \frac{v_{ab}+v_{ac}}{3} + j\frac{v_{bc}}{\sqrt{3}} \tag{16}$$

A common $d_s - q_s$ to $\alpha-\beta$ frame conversion transformation, $\underline{i}_{\alpha\beta} = \underline{i}_{dq} e^{j\hat{\theta}_s}$, can now be applied to derive:

$$\hat{i}_{s\alpha} = \hat{i}_{sd}\cos(\hat{\theta}_r - \theta_p) - \hat{i}_{sq}\sin(\hat{\theta}_r - \theta_p), \tag{17}$$

$$\hat{i}_{s\beta} = \hat{i}_{sd}\sin(\hat{\theta}_r - \theta_p) + \hat{i}_{sq}\cos(\hat{\theta}_r - \theta_p), \tag{18}$$

where $\hat{\theta}_s = \hat{\theta}_r - \theta_p$ (Figure 4(B)) and $\hat{\theta}_r = p_r\hat{\theta}_{rm}$ are the estimated secondary frame and rotor 'electrical' positions.

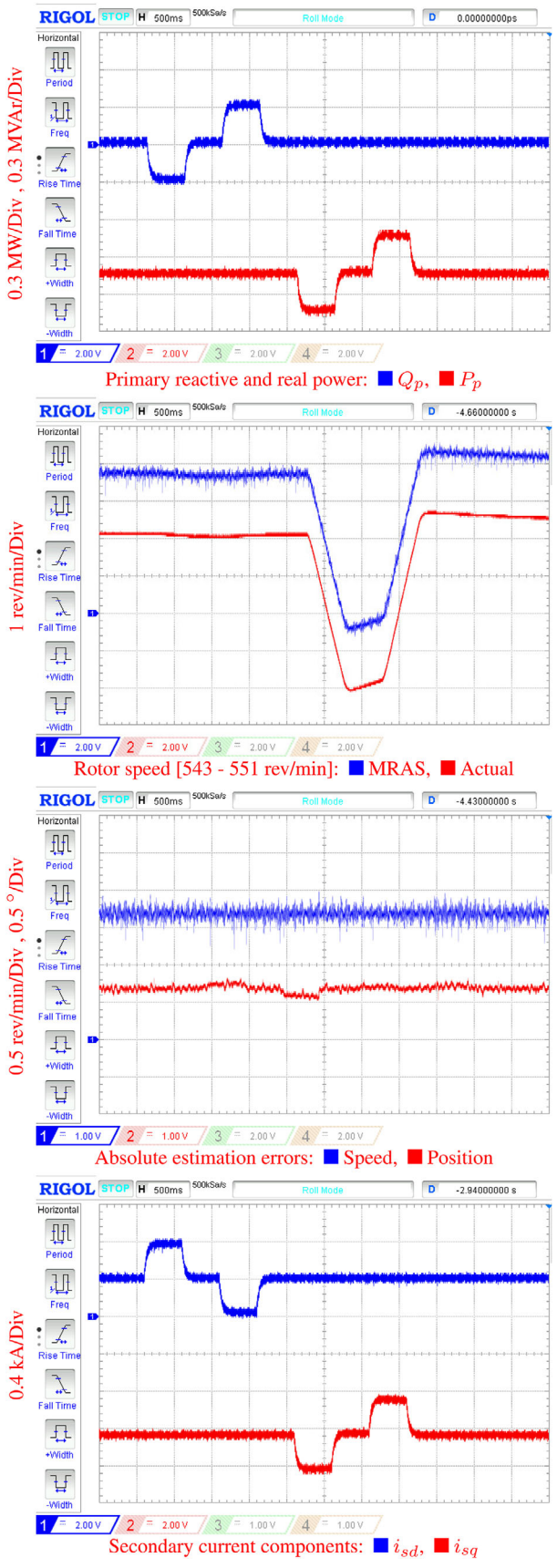

FIGURE 15 Oscillograms of the BDFRG and controller response to sudden primary power variations at 11 m/s wind speed

The error between the reference and adaptive model outputs is defined as the cross product of the true and estimated secondary-current vectors of the form:

$$\varepsilon = \frac{\hat{\underline{i}}_s \times \underline{i}_s}{i_s^2} = \frac{\hat{i}_s \cdot i_s}{i_s^2} \sin\delta_{err} = \frac{\hat{i}_{s\alpha} i_{s\beta} - \hat{i}_{s\beta} i_{s\alpha}}{i_{s\alpha}^2 + i_{s\beta}^2}, \tag{19}$$

where $\delta_{err} = \delta - \hat{\delta}$ is their angular phase displacement (Figure 4(B)). By continuously updating the adaptive model with the improved position estimates as shown in Figure 4(B), δ_{err} should eventually converge to zero when the estimated ($\hat{i}_s$) and actual (i_s) current vectors overlap both rotating at ω_s. An adaptive scheme is developed on the basis of a small signal analysis of ε with the following approximations in steady-state, $\delta_{err} \approx 0$, $\cos\delta_{err} \approx 1$ and $\hat{i}_s \approx i_s$:

$$\frac{d\varepsilon}{dt} = \dot{\varepsilon} = \frac{\hat{i}_s \cdot i_s}{i_s^2} \cos\delta_{err} \left(\frac{d\delta}{dt} - \frac{d\hat{\delta}}{dt} \right) \approx \frac{d\delta}{dt} - \frac{d\hat{\delta}}{dt},$$

$$\approx \omega_s - \hat{\omega}_s = (\omega_r - \omega_p) - (\hat{\omega}_r - \omega_p) = \Delta\omega r, \tag{20}$$

$$\varepsilon \approx \int (\omega_r - \hat{\omega}_r)\, dt = \frac{\omega_r - \hat{\omega}_r}{s} = \frac{\Delta\omega_r}{s}. \tag{21}$$

A prerequisite for the small-signal stability of the closed-loop MRAS observer (i.e $\dot{\varepsilon} \approx 0$) would be satisfied if $\Delta\omega_r \approx 0$ in Equation (20). The required damping and zero steady-state error for the estimation response are achieved by using a PI as the adaptation mechanisms for MRAS [35]. This PI controller is designed based on Equation (21) to drive ε to zero. Dividing ε by i_s^2 provides a straightforward on-line adaptive PI tuning under variable loading conditions of the BDFRG. The raw angular velocity estimates ($\hat{\omega}_r$) generated by the observer are further processed using a low-pass filter to improve the quality of the corresponding mechanical output ($\hat{\omega}_{rm}$), which is necessary for accurate MPPT as illustrated in Figures 4(A) and 5(A).

The $\hat{\theta}_r$ is estimated by integrating the $\hat{\omega}_r$ signal by analogy to a conventional technique used for incremental encoders. A conventional PLL, shown in Figure 4(A), is used to obtain the angular frequency (ω_p) and phase (θ_p) of sinusoidal three-phase primary voltages in a rotating $d-q$ frame as detailed in ref. [36]. This PLL is designed for normal stiff grid conditions considered in this paper, and it can effectively eradicate noise and dc-offset in voltage measurements. The impact of weak grids on the PLL performance is studied in refs. [37, 38] and the corresponding methods are presented in ref. [39].

4.2 | Parameter knowledge uncertainties

The machine parameter dependence of the adaptive model is evident from Equations (14)–(18) used to estimate the secondary $\alpha\beta$ currents. Therefore, any mismatch between the applied ($\hat{L}_{m,p}$) and actual $L_{m,p}$ values, caused by off-line testing inaccuracies, magnetic saturation or otherwise, can influence the

observer performance in different ways. For instance, the $\hat{i}_{sq}$ and $\hat{i}_{sd}$ estimates using Equations (14) and (15) are prone to errors in $\hat{L}_p/\hat{L}_m$, the latter also being affected by $\hat{L}_m$. The situation is even worse for $\hat{i}_{s\alpha}$ and $\hat{i}_{s\beta}$ coming from Equations (17) and (18) where further estimation inaccuracies can be introduced by erroneous $\hat{\theta}_r$. In order to illustrate the effects of all these variations on the position estimation quality, Equations (17) and (18) can be manipulated into a more insightful single equation of the form:

$$\tan(\hat{\theta}_r - \theta_p) = \tan\hat{\theta}_s = \frac{\frac{\hat{i}_{sd}}{\hat{i}_{sq}}\tan\hat{\delta} - 1}{\frac{\hat{i}_{sd}}{\hat{i}_{sq}} + \tan\hat{\delta}}, \tag{22}$$

where using Equations (14) and (15):

$$\frac{\hat{i}_{sd}}{\hat{i}_{sq}} = \frac{3v_p^2}{2\omega_p\hat{L}_p P_p} - \frac{Q_p}{P_p} = \frac{V_p^2}{\hat{X}_p P_p} - \frac{Q_p}{P_p}, \tag{23}$$

Substituting now for Equation (23), Equation (22) can be further developed as follows:

$$\tan(\underbrace{\hat{\theta}_r - \theta_p}_{\hat{\theta}_s}) = \frac{V_p^2\tan\hat{\delta} - \hat{X}_p\cdot(Q_p\tan\hat{\delta} + P_p)}{V_p^2 + \hat{X}_p\cdot(P_p\tan\hat{\delta} - Q_p)}. \tag{24}$$

The MRAS satisfies Equation (24) by maintaining $\varepsilon \approx 0$ in steady-state regardless of the inductance mismatch. Thus, the estimated ($\hat{i}_s$) and actual (i_s) secondary current vectors are always nearly in phase (i.e. $\delta_{err} \approx 0$) rotating at the same velocity $\hat{\omega}_s \approx \omega_s$, albeit with different magnitudes ($\hat{i}_s \neq i_s$) as shown in Figure 4(B) so that $\hat{\delta} \approx \delta$ or:

$$\tan\hat{\delta} = \frac{\hat{i}_{s\beta}}{\hat{i}_{s\alpha}} \approx \tan\delta = \frac{i_{s\beta}}{i_{s\alpha}} \Leftrightarrow \frac{\hat{i}_{s\beta}}{i_{s\beta}} \approx \frac{\hat{i}_{s\alpha}}{i_{s\alpha}} \approx \frac{\hat{i}_s}{i_s} \neq 1. \tag{25}$$

The wrong $\hat{L}_p$ causes the rotor position estimation ($\hat{\theta}_r$) errors, which can be understood from Equations (22)–(24). Namely, with the $\tan\hat{\delta}$ estimates being fairly accurate by the MRAS strategy as mentioned above, the $\hat{\theta}_r$ inaccuracies coming from Equations (22) and (24) are essentially induced by the incorrect $\hat{i}_{sd}/\hat{i}_{sq}$ due to the erroneous $\hat{X}_p = \omega_p\hat{L}_p$ values in Equation (23) considering that both the line-to-line rms voltage (V_p) and angular frequency (ω_p) are fixed by the primary winding grid connection. It may be easily concluded from Equations (23) and (24) that for a given operating point determined by P_p and Q_p, the larger the $\hat{X}_p$, the lower $\hat{i}_{sd}/\hat{i}_{sq}$ and $\hat{\theta}_r$ become. Therefore, in case of deviations from the exact X_p, a smaller $\hat{\theta}_r$ error ($\Delta\theta_r$) would be produced if $\hat{X}_p > X_p$ than for $\hat{X}_p < X_p$. Also, note from Equation (22) that since $\hat{\theta}_r - \theta_p = \hat{\theta}_s$, $\Delta\theta_r$: Equation (1) propagates to Equations (17) and (18) bringing additional errors in $\hat{i}_{s\alpha}$ and $\hat{i}_{s\beta}$ making $\hat{i}_{s\alpha} \neq i_{s\alpha}$, $\hat{i}_{s\beta} \neq i_{s\beta}$, hence $\hat{i}_s \neq i_s$ within the constraints defined by Equation (25); Equation (2) manifests itself as a misalignment between the estimated ($\hat{d}_s - \hat{q}_s$) and actual ($d_s - q_s$) secondary frames (Figure 4(B)) as formulated below:

$$\Delta\theta_r = \theta_r - \hat{\theta}_r = (\theta_s + \theta_p) - (\hat{\theta}_s + \theta_p) = \theta_s - \hat{\theta}_s = \Delta\theta_s \tag{26}$$

5 | SIMULATION RESULTS

The MRAS observer (Figure 4(A)) is applied to achieve the sensorless control (Figure 2(A)) of the BDFRG-based WECS (Figure 5(A)) simulated in Simulink®. The following practical effects were incorporated to make the simulations as realistic as possible: discrete-time implementation, high frequency white noise and transducer dc offset in the measured signals, and detailed IGBT power-electronics converter models. A family of typical GE®turbine characteristics for various wind and generator speeds, including the MPPT trajectory, used for the simulation studies are displayed in Figure 5(B) [40, 41]. The BDFRG wind turbine specifications can be found in Table 1 and its optimised 'ducted' rotor design details (Figure 3) in ref. [9].

5.1 | Variable speed wind energy conversion

Figure 6 illustrates the precise rotor speed ($\hat{n}_{rm}$) and position ($\hat{\theta}_r$) estimation and effective power control in a desired base speed range of the WECS. The wind profile with a fast slew rate of ±1 m/s is chosen to examine the MRAS observer performance during deceleration from 600 rev/min through the synchronous 500 rev/min and down to 350 rev/min followed by an acceleration back to the rated 600 rev/min. The absolute speed error (Δn_{rm}) does not exceed 2.5 rev/min with about 1 rev/min mean throughout. This small dc offset has been introduced by the first-order low-pass filter used to handle the noisy $\hat{\omega}_r/p_r$ estimates coming from the observer (Figure 4(A)) as shown in the zoomed snapshot on the speed sub-plot. Such a filtering has been necessary for reliable MPPT as per Figure 5(A). The $\hat{\theta}_r$ values for the observed $\hat{\omega}_r$ are accurate to $\Delta\theta_r \approx 0.6°$ electrical and p_r times less, i.e. 0.1° mechanical (not shown), in average. For this test, the BDFRG is operated at unity power factor ($Q_p^{ref} = 0$ in Figure 2(A)) resulting in the virtually constant $i_{sd} \approx 0.4$ kA and zero i_{pd} given Equation (12) with the machine magnetisation being entirely provided from the secondary side. The power producing i_{sq} and i_{pq} change proportionally to the P_p variations considering Equation (11). Note that the secondary power (P_s) is indeed bi-directional in nature as indicated in Figure 3 to balance out the difference between the required MPPT reference input (P_m^{ref}) and respective primary winding share (P_p^{ref}) according to Equation (3) and Figure 5(A). The P_s waveform shows that the BDFRG converter injects power (i.e. $P_s < 0$) to the grid in the super-synchronous region (i.e. above 500 rev/min)

and consumes (i.e. $P_s > 0$) in the sub-synchronous mode (i.e. below 500 rev/min). The adaptive model can obviously produce the majority of quality $\hat{i}_{s\alpha}$ and $\hat{i}_{s\beta}$ outputs judging by $|i_s - \hat{i}_s| \approx 0.01$ kA and $|\delta_{err}| \leq 1°$ (Figure 4(B)) in average sense. Such a high estimation accuracy, coupled with very little error in $\hat{\theta}_r$, hence the secondary frame angles ($\hat{\theta}_s$) bearing in mind Equation (26), imply the smooth, intrinsically decoupled power (current) control as expected from Equations (11) and (12). This can be clearly seen from the P_p and Q_p curves, and the closely related $i_{sq} \approx i_{pq}$ and $i_{sd} \approx i_{pd}$ counterparts, on the pertaining sub-plots. Another important observation from an operational point of view is certainly the secondary winding phase sequence reversal from positive to negative (and vice-versa while riding through the synchronous speed around 110 s this transient being difficult to see clearly with the scaling adopted) during the speed mode transition around 35 s time instant corresponding to $\omega_s < 0$ in Equations (1) and (3) and Figure 3.

5.2 | Disturbance rejection evaluation

Since the adaptive model relies on the current–power expressions (14) and (15) to estimate the secondary current stationary frame components given by Equations (17) and (18), the MRAS observer is subjected to P_p and Q_p step changes to test its robustness at a constant wind speed. Figure 7 shows that sudden ±0.3 MVAr/MW variations in the respective power references (Figure 5(A)) do not affect the marginal estimation errors similar to those in Figure 6. The observer strong disturbance rejection properties reflect upon the apparently stable and decoupled power (current) control, which is visible from the $P_p \approx i_{sq}$ and $Q_p \approx i_{sd}$ waveforms by analogy to Figure 6. It is important to emphasise that $i_{sd}^{ref} = 0.4$ kA and $i_{sq}^{ref} = -1.32$ kA calculated using Equations (12) and (11) for $Q_p^{ref} = 0$ MVAr and $P_p^{ref} = -1.05$ MW and the BDFRG parameters in Table 1 are fully consistent with the readings from the respective plots in Figures 6 and 7 despite the fact that the BDFRG specifications are unknown to the PI regulators in Figure 2(A) illustrating their very good response.

Figure 8 presents another convincing evidence of the excellent BDFRG and sensorless controller performance prospects this time considering a realistic wind speed profile with the following data: maximum, minimum and average value of 12.6 m/s, 7.0 m/s, and 9.8 m/s, respectively. The high $\hat{n}_{rm}$ and $\hat{\theta}_r$ estimation accuracy is retained throughout regardless of the wind fluctuations, and so is the decoupled Q_p control which is largely unaffected by the speed dependent P_p variations in much the same manner as in Figure 6.

5.3 | Parameter sensitivity studies

The latest evaluation of the existing parameter identification methods for a 8/4-pole BDFRG similar to that in Figure 3 has been made in ref. [30]. It has been found that a less than 10% correlation generally exists between the laboratory tests and finite elements analyses predictions for L_m, and below 5% for L_p. Yet, a mismatch ranging from −30% to 10% has been assumed in $\hat{L}_m$ and ±20% in $\hat{L}_p$ to assess the MRAS observer robustness potential. A fixed wind speed of 11 m/s and ±0.3 MVAr/MW step changes in the power reference signals have been simulated under the same operating conditions as in Figure 7, generated using the exact L_m and L_p from Table 1, for comparisons.

Figure 9 shows the results when 30% and 20% reductions relative to the actual L_m and L_p of the BDFRG have been applied for the MRAS observer calculations (i.e. $\hat{L}_m = 0.7L_m$ and $\hat{L}_p = 0.8L_p$). The adaptive model, structured around Equations (19)–(21), maintains $\varepsilon \approx 0$ under all circumstances making the maximum $|\delta_{err}| < 1.4°$ and only about 0.6° in average, whereas $\Delta n_{rm} \approx 2$ rev/min or less. It should be noted that these figures are all near or at the 'ideal' levels in Figure 7 no matter the significant deviations in $\hat{L}_m$ and $\hat{L}_p$. However, the underestimated $\hat{L}_m$ has a trade-off in the more pronounced sensitivity of Equations (14) and (15), the latter in particular as being only dependent on and inversely proportional to $\hat{L}_m$ for $Q_p^{ref} = 0$, hence increased errors in $\hat{i}_{sq}$ but foremost $\hat{i}_{sd}$, and further in $\hat{i}_{s\alpha}$ and $\hat{i}_{s\beta}$ through Equations (17) and (18), and finally $|i_s - \hat{i}_s| \approx 0.23$ kA in average. The higher mean $\Delta\theta_r \approx 4°$, with $\hat{\theta}_r$ taking part in Equations (17) and (18), is another contributing factor to the $\hat{i}_s$ digression. It is important to point out that $\Delta\theta_r$, which is carried over to the secondary frame angular misalignment ($\Delta\theta_s$) given Equation (26), is exclusively a consequence of $\hat{L}_p$ underestimation according to Equation (24) as detailed in Section 4.2. Although the accuracy of $\hat{i}_s$ and $\hat{\theta}_r$ estimates has worsened compared to the situation in Figure 7, the controller performance do not appear to be influenced by the relatively small $\Delta\theta_s \approx 4°$ incurred as demonstrated by the $P_p \approx i_{sq}$ and $Q_p \approx i_{sd}$ responses, which precisely follow their set points in a decoupled fashion.

The implications of the $\hat{L}_m = 1.1L_m$ and $\hat{L}_p = 1.2L_p$ case study are presented in Figure 10. A very similar estimation and decoupled control quality to that in Figure 9 has been obtained with the observer inherent immunity to inductance variations when it comes to $\hat{n}_{rm}$ and $\hat{\delta}$ predictions (Figure 4(B)). Furthermore, the $\Delta\theta_r = \Delta\theta_s$ has gone down to 3°, i.e. by about 25% from its average value in Figure 9, and $|i_s - \hat{i}_s|$ more than halved to ≈ 0.1 kA. Such a notable improvement in the accuracy of estimates can be explained by the much lower sensitivity of the underlying expressions, referenced in the preceding paragraph, to the overestimated than the underestimated inductance values.

The results in Figure 11 are complementary to those in Figure 8 and are generated for the same wind speed conditions to investigate separately the effects of $\hat{L}_m$ underestimation as being more challenging for the observer to face in terms of the sensitivity issues. Another purpose is to examine the controller disturbance rejection capabilities to Q_p^{ref} step changes not shown in Figure 8. The position error plots ($\Delta\theta_r = \Delta\theta_s$) in the two figures are absolutely identical proving that both $\hat{\theta}_r$ and $\hat{\theta}_s$ estimates are totally independent of $\hat{L}_m$ variations as expected from Equation (24). A similar observation can be made for $\hat{n}_{rm}$, which exhibits only about 1 rev/min difference from the val-

ues estimated using the exact L_m in Figure 8. The mismatched $\hat{L}_m$ produces higher $|i_s - \hat{i}_s|$ than in Figure 8 for the very same reasons as elaborated with regard to Figure 9. However, this causes no apparent performance degradation at such a small $\Delta\theta_s \approx 0.5°$ in average, and given the fact that the measured (and not estimated) secondary currents are used to generate the i_{sd} and i_{sq} feedback components for power (current) control as shown in Figure 2(A). Therefore, it can be concluded that the estimation accuracy of the observer key outputs, including $\hat{n}_{rm}$ responsible for the MPPT and $\hat{\theta}_s$ determining the power control quality, is predominantly dictated by the $\hat{L}_p$ sensitivity. Finally, it can be seen that the P_p waveform in Figure 11 is virtually a replica of that in Figure 8, and hence clearly undisturbed by the varying Q_p as expected from decoupled control. The same applies to the corresponding i_{sq} profile showing no obvious signs of any disruption in response to the Q_p related i_{sd} pulses.

5.4 | Primary winding resistance effects

The influence of resistance (R_p) variations on the MRAS observer response is presented in Figure 12. The R_p value used in the generator model is increased by as much as 200% within 1 s time interval to mimic the real-time temperature rise of R_p. The BDFRG is operated assuming a constant wind speed of 11 m/s, and an active power disturbance is introduced similarly to Figure 7. This test shows that despite doubling the resistance, the robustness and stability of the MRAS observer remain unaffected.

5.5 | Stability analysis of MRAS observer

As explained in Section 4, the MRAS performance depends on the the adaptation mechanism. The ε values coming from Equation (19) are plotted in Figure 13 for variable speed (Figure 6), power disturbance (Figure 7) and parameter mismatches (Figures 9 and 10) conditions as indicated by the respective y-axis labels on the graphs. A comparison of the results presented reveals that the designed PI regulator is capable of maintaining ε very close, and down to zero in average (denoted by yellow lines) preserving the observer stability throughout.

6 | EXPERIMENTAL VERIFICATION

The real-time performance of the MRAS-based sensorless control of the 1.5 MW BDFRG WECS is evaluated by the Hardware-In-the-Loop (HIL) tests as shown in Figure 14. The algorithm in Figure 2(A) is implemented and executed in dSPACE®[42] at 10 kHz. The experimental results presented in Figure 15 clearly demonstrate the excellent disturbance rejection features of the controller and high observer accuracy. The measured rotor speed and position errors are only 1.6 rev/min and 0.75°, respectively, which are well in line with the corresponding simulations in Figure 7 discussed in Section 5.2. Moreover, the simulated and HIL waveforms of the decoupled control of primary real and reactive power, as well as the closely related secondary qd currents given Equations (12) and (11), and the BDFRG speed are also very similar in magnitude, as can be seen when comparing the plots in Figures 7 and 15, both in steady-state and during transients.

7 | CONCLUSIONS

A novel, robust MRAS observer for sensorless MPPT and reactive power control of the emerging, medium-speed BDFRG wind turbine technology for grid-connected applications has been proposed and supported by the comprehensive parameter sensitivity studies. By virtue of its optimal configuration built upon a small signal analysis, the observer has been proven capable of producing accurate rotor speed and position estimates avoiding the use of a shaft-encoder. The realistic simulation results for a large-scale custom-designed BDFRG prototype have been underpinned by the real-time HIL experiments showing a very promising controller performance potential. The observer merits and contributions of this paper can be summarised in the following main aspects:

- The MRAS observer is centred around a transducer accurate, parameter-free reference model using the secondary current measurements only, which makes a strong foundation for the algorithm convergence. From this point of view, it provides prospects to outperform the secondary flux or reactive power based observers for the BDFRG in terms of the estimation accuracy and functional stability.
- The adaptive model brings another significant advantage by deriving the rotor-position dependent secondary-current components from the measured grid voltages and currents. Although $\hat{L}_m$ and $\hat{L}_p$ have to be known for this purpose, the calculations are done at fixed line voltage and frequency, allowing one to obtain quality, inverter switching ripple free estimates improving the observer reliability.
- Neglecting the small R_p with large generators has greatly simplified the primary flux identification and the observer/controller design itself by avoiding the voltage integration and filtering requirements.
- Apart from the R_p, the observer is also completely independent of all the secondary winding quantities, which are either highly susceptible to estimation errors due to sensitivity issues (e.g. flux, $\hat{L}_s$) or they can not be measured directly (e.g. terminal PWM inverter voltages).
- The stationary frame secondary current angle and the rotor angular velocity ($\hat{\omega}_{rm}$) estimates are unaffected by the $\hat{L}_{m,p}$ uncertainties, and as such always highly accurate so is the $\hat{\omega}_{rm}$ dependent MPPT.
- The observation process is generally much less sensitive to the over-estimated than the under-estimated inductances, either $\hat{L}_m$ or $\hat{L}_p$. Hence, it is more accurate in the former case.

- The rotor position errors are replicated to the secondary frame misalignment, i.e. $\Delta\theta_r = \Delta\theta_s$. They are only caused by the $\hat{L}_p$ variations and have nothing to do with $\hat{L}_m$.
- The stationary $\alpha - \beta$ frame secondary currents predictions are the most erroneous in nature as being simultaneously influenced by the estimation inaccuracies of multiple parameters, including the rotor position and individual secondary frame $d - q$ current components.
- The MPPT and reactive power PI control is inherently decoupled with excellent disturbance rejection features over the considered speed range typical for WECS. It is parameter independent in its own right, thus largely robust to the inductance mismatches.

The good results obtained are certainly highly encouraging to warrant further investigations of this viable DFIG alternative for variable speed wind turbines. It is believed that with its enhanced reliability of brushless structure, maintenance-free sensorless operation, and the use of a compact 2-stage gearbox, the BDFRG can be an appealing cost-effective option for future WECS drive trains.

ORCID

Mohammad-Reza Agha-Kashkooli https://orcid.org/0000-0001-7537-5497

REFERENCES

1. Fischer, K., et al.: Reliability of power converters in wind turbines: Exploratory analysis of failure and operating data from a worldwide turbine fleet. IEEE Trans. Power Electron. 34(7), 6332–6344 (2019)
2. Oraee, A., Abdi, E., McMahon, R.A.: Converter rating optimisation for a brushless doubly fed induction generator. IET Renew. Power Gener. 9(4), 360–367 (2015)
3. Han, P., et al.: Brushless doubly-fed machines: Opportunities and challenges. Chin. J. Electr. Eng. 4(2), 1–17 (2018)
4. Zhang, F., et al.: Design and performance comparisons of brushless doubly-fed generators with different rotor structures. IEEE Trans. Ind. Electron. 66(1), 631–640 (2019)
5. Abdi, E., et al.: Performance analysis and testing of a 250 kW medium-speed brushless doubly-fed induction generator. IET Renew. Power Gener. 7(6), 631–638 (2013)
6. Cheng, M., et al.: Emerging multiport electrical machines and systems: Past developments, current challenges, and future prospects. IEEE Trans. Ind. Electron. 65(7), 5422–5435 (2018)
7. Rini Ann Jerin, A., et al.: Review on FRT solutions for improving transient stability in DFIG-WTs. IET Renew. Power Gener. 12(15), 1786–1799 (2018)
8. Tohidi, S.: Analysis and simplified modelling of brushless doubly-fed induction machine in synchronous mode of operation. IET Electr. Power Appl. 10(2), 110–116 (2016)
9. Attya, A.B., et al.: Frequency support using doubly fed induction and reluctance wind turbine generators. Int. J. Electr. Power Energy Syst. 101, 403–414 (2018)
10. Hsieh, M.F., Chang, Y.H., Dorrell, D.: Design and analysis of brushless doubly-fed reluctance machine for renewable energy applications. IEEE Trans. Magn. 52(7), (2016)
11. Zhang, F., et al.: Effects of design parameters on performance of brushless electrically excited synchronous reluctance generator. IEEE Trans. Ind. Electron. 65(11), 9179–9189 (2018)
12. Gorginpour, H., Jandaghi, B., Oraee, H.: A novel rotor configuration for brushless doubly-fed induction generators. IET Electric Power Appl. 7(2), 106–115 (2013)
13. McMahon, R.A., et al.: Design considerations for the brushless doubly-fed (induction) machine. IET Electric Power Appl. 10(5), 394–402 (2016)
14. Zhang, F., et al.: Rotor optimisation design and performance comparison of BDFG for wind power generation. IET Electric Power Appl. 13(3), 370–378 (2019)
15. Rebeiro, R.S., Knight, A.M.: Design and torque capability of a ducted rotor brushless doubly fed reluctance machine. IET Electric Power Appl. 12(7), 1058–1064 (2018)
16. Jovanović, M.: Sensored and sensorless speed control methods for brushless doubly fed reluctance motors. IET Electric Power Appl. 3(6), 503–513 (2009)
17. Jovanović, M., Chaal, H.: Wind power applications of doubly-fed reluctance generators with parameter-free hysteresis control. Energy Convers. Manage. 134, 399–409 (2017)
18. Zhu, L., et al.: Optimized power error comparison strategy for direct power control of the open-winding brushless doubly fed wind power generator. IEEE Trans. Sustainable Energy 10(4), 2005–2014 (2019)
19. Ademi, S., Jovanović, M.G.: Vector control methods for brushless doubly fed reluctance machines. IEEE Trans. Ind. Electron. 62(1), 96–104 (2015)
20. Ademi, S., Jovanović, M.G., Hasan, M.: Control of brushless doubly-fed reluctance generators for wind energy conversion systems. IEEE Trans. Energy Convers. 30(2), 596–604 (2015)
21. Cardenas, R., et al.: Overview of control systems for the operation of DFIGs in wind energy applications. IEEE Trans. Ind. Electron. 60(7), 2776–2798 (2013)
22. Susperregui, A., et al.: Automated control of doubly fed induction generator integrating sensorless parameter estimation and grid synchronisation. IET Renew. Power Gener. 8(1), 76–89 (2014)
23. Bayhan, S., Abu-Rub, H., Ellabban, O.: Sensorless model predictive control scheme of wind-driven doubly fed induction generator in DC microgrid. IET Renew. Power Gener. 10(4), 514–521 (2016)
24. Chibah, A., et al.: Experimental design of a new fast sensorless control of DFIG in complex domain. IET Electric Power Appl. 13(5), 581–593 (2019)
25. Ademi, S., et al.: A new sensorless speed control scheme for doubly fed reluctance generators. IEEE Trans. Energy Convers. 31(3), 993–1001 (2016)
26. Jovanovic, M., Ademi, S., Binns, R.: Sensorless variable speed operation of doubly-fed reluctance wind generators. IET Renew. Power Gener. 1–10 (2020)
27. Kiran, K., et al.: Sensorless speed control of brushless doubly-fed reluctance motor drive using secondary flux based MRAS. Electr. Power Compon. Syst. 46(6), 701–715 (2018)
28. Kiran, K., Das, S.: Implementation of reactive power-based MRAS for sensorless speed control of brushless doubly fed reluctance motor drive. IET Power Electron. 11(1), 192–201 (2018)
29. Kumar, M., Das, S., Kiran, K.: Sensorless speed estimation of brushless doubly-fed reluctance generator using active power based MRAS. IEEE Trans. Power Electron. 34(8), 7878–7886 (2019)
30. Gay, D., et al.: Brushless doubly fed reluctance machine testing for parameter determination. IEEE Trans. Ind. Appl. 55(3), 2611–2619 (2019)
31. Agha Kashkooli, M.R., Jovanović, M.G.: A MRAS observer for sensorless operation of grid-connected BDFRG wind turbines. 2020 IEEE 29th International Symposium on Industrial Electronics (ISIE), pp. 1517–1522, IEEE, Piscataway, NJ (2020)

32. Agha Kashkooli, M.R., Jovanović, M.G., Ademi, S.: Sensorless power control of doubly-fed reluctance wind turbine generators using a current-based mras estimator. 2020 International Symposium on Power Electronics, Electrical Drives, Automation and Motion (SPEEDAM), pp. 65–70, IEEE, Piscataway, NJ (2020)
33. Carroll, J., McDonald, A., McMillan, D.: Reliability comparison of wind turbines with DFIG and PMG drive trains. IEEE Trans. Energy Convers. 30(2), 663–670 (2015)
34. Betz, R.E., Jovanović, M.G.: Introduction to the space vector modelling of the brushless doubly-fed reluctance machine. Electr. Power Compon. Syst. 31(8), 729–755 (2003)
35. Nguyen, N.T.: Model-Reference Adaptive Control, A Primer. Springer, Cham (2018)
36. Abad, G., et al.: Doubly Fed Induction Machine: Modeling and Control for Wind Energy Generation Applications, 1st Ed., Wiley-IEEE Press, Hoboken, NJ (2011)
37. Xi, X., Geng, H., Yang, G.: Enhanced model of the doubly fed induction generator-based wind farm for small-signal stability studies of weak power system. IET Renew. Power Gener. 8(7), 765–774 (2014)
38. Liu, J., et al.: Impact of power grid strength and pll parameters on stability of grid-connected dfig wind farm. IEEE Trans. Sustainable Energy 11(1), 545–557 (2020)
39. Golestan, S., et al.: dq-frame cascaded delayed signal cancellation- based pll: Analysis, design, and comparison with moving average filter-based pll. IEEE Trans. Power Electron. 30(3), 1618–1632 (2015)
40. Lorenzo-Bonache, A., et al.: Generic type 3 WT models: Comparison between IEC and WECC approaches. IET Renew. Power Gener. 13(7), 1168–1178 (2019)
41. Hemanth Kumar, M.B., et al.: Review on control techniques and methodologies for maximum power extraction from wind energy systems. IET Renew. Power Gener. 12(14), 1609–1622 (2018)
42. DS1103 PPC Controller Board: Hardware Installation and Configuration. dSPACE GmbH, Paderborn, Germany (2014). www.manualslib.com/manual/1666045/Dspace-Ds1103.html. Accessed 26 November 2020

How to cite this article: Agha-Kashkooli M-R, Jovanović M. Sensorless MRAS control of emerging doubly-fed reluctance wind generators. *IET Renew. Power Gener.* 2021;15:2007–2021.
https://doi.org/10.1049/rpg2.12123